Research in Astronomy and Astrophysics, 22:115002 (15pp), 2022 November https://doi.org/10.1088/1674-4527/ac8d80

Spectral and Timing Analysis of the Black Hole Transient MAXI J1631–479 During its 2019 Outburst Observed with Insight-HXMT

Yu-Cong Fu[1,2,3], L. M. Song[3], G. Q. Ding[1], S. N. Zhang[3], J. L. Qu[3], S. Zhang[3], L. Zhang[3], Q. C. Bu[4], Y. Huang[3], X. Ma[3], Z. X. Yang[2,3], Y. L. Tuo[3], X. F. Lu[3], D. K. Zhou[2,3], B. Y. Wu[2,3], T. M. Li[2,3], and Y. C. Xu[2,3]
[1] Xinjiang Astronomical Observatory, Chinese Academy of Sciences, Urumqi, Xinjiang 830011, China; fuyucong@xao.ac.cn, dinggq@xao.ac.cn
[2] University of Chinese Academy of Sciences, Chinese Academy of Sciences, Beijing 100049, China
[3] Key Laboratory of Particle Astrophysics, Institute of High Energy Physics, Chinese Academy of Sciences, Beijing 100049, China; songlm@ihep.ac.cn
[4] Institut für Astronomie und Astrophysik, Kepler Center for Astro and Particle Physics, Eberhard Karls Universität, Sand 1, D-72076 Tübingen, Germany
Received 2022 July 7; revised 2022 August 3; accepted 2022 August 25; published 2022 October 12

Abstract

We report spectral and timing analysis of the black hole transient MAXI J1631–479 during the hard intermediate state of its 2019 outburst from the Insight-Hard X-ray Modulation Telescope (Insight-HXMT) observations. We find that the energy dependence of the type-C quasi-periodic oscillation (QPO) frequency evolves with time: during the initial rise of a small flare (∼MJD 58526.0-58527.1), the QPO frequency increases with increasing energy from ∼1 to ∼100 keV, and then the frequency remains constant after MJD 58527.1. We discover a possible new phenomenon of Fe line's QPO frequency jump that has never been observed for other black hole transients: during the small flare, the QPO frequency around the Fe line energy is higher than any other energy band, with the frequency difference $\Delta f = 0.25 \pm 0.08$ Hz between 5.5–7.5 keV and other energy bands. The spectral analysis shows that the evolution of QPOs is related to the equivalent width of the narrow Fe line, and its equivalent width increases during this small flare. We propose that the QPO frequency difference results from the differential precession of a vertically extended jet, and the higher QPO frequency of Fe line could be caused by the layered jet when the jet scale increases. At the same time, the evolution of QPOs is related to the accretion rate, while the energy dependence of QPOs supports the existence of deceleration in the vertically distributed jet.

Key words: accretion – accretion disks – stars: black holes – X-rays: binaries

1. Introduction

Black hole transients (BHTs) are mostly low-mass X-ray binaries (LMXBs), which spend most of their lives in quiescence. During a typical outburst, lasting from months to years, they display apparent evolution in their X-ray spectral and timing properties. They usually start an outburst from the low hard state (LHS), go through the hard and soft intermediate states (HIMS, SIMS), enter the high soft state (HSS), then go through again the intermediate states and return to the LHS (Belloni 2010; Remillard & McClintock 2006; Belloni & Motta 2016). Low frequency quasi-periodic oscillations (LFQPOs) are generally observed in BHTs, classified as A, B and C types (Remillard et al. 2002; Casella et al. 2005). They are observed as narrow peaks in the power density spectra (PDSs), with frequency varying from a few millihertz to dozens of hertz. The relation between spectral evolution and X-ray variability has been studied in lots of work, and there is a close connection between spectral state and the characteristics of LFQPOs (Belloni et al. 2005, 2011).

The X-ray radiation produced by BHTs comes mainly from blackbody radiation from the accretion disk and inverse Compton scattering from the hot and optically thin corona. In the LHS, the X-ray spectrum is thought to be dominated by a non-thermal emission arising from the Comptonization of soft disk photons in a hot and optically thin corona (Done et al. 2007; Gilfanov 2010; Belloni & Motta 2016). In the HIMS, the disk component starts to become important. In both the LHS and HIMS, superposed on a strong flat top noise (FTN), type-C quasi-periodic oscillations (QPOs) are commonly observed, which are characterized in the PDS by a high amplitude (up to ∼16% rms) and narrow (the coherence parameter $Q \sim 7$–12) peak (Vignarca et al. 2003; Casella et al. 2005). The appearance of type-B QPOs means that the source has entered the SIMS, while they have a relatively high amplitude (up to ∼4% rms), narrow ($Q \leqslant 3$) peak and a weak red noise, but do not have FTN (Remillard et al. 2002; Casella et al. 2005). When the source transitions into HSS from SIMS, the X-ray spectrum is dominated by the soft disk component; the PDS shows weak red noise and type-A QPOs, which are characterized by a weak and broad peak. The origin of LFQPOs is still under debate, and it is essential to study the LFQPOs for our understanding of the accretion process around black holes. Several models have been proposed to explain the dynamical origin of type-C QPOs (Stella & Vietri 1998;

Schnittman et al. 2006; Cabanac et al. 2010; Ingram et al. 2009), and one of the promising models is that type-C QPOs are produced by Lense-Thirring (LT) precession of the inner accretion flow (Ingram et al. 2009). Alternatively, a model based on the LT precession of a small-scale jet describes the origin of type-C QPOs in MAXI J1820+070 (Ma et al. 2021). The origin of type-B QPO has been connected to the emission arising from the relativistic jet (Fender et al. 2009; Homan et al. 2020; Russell et al. 2020; Zhang et al. 2021). A two-Comptonization model successfully explains both the time-averaged spectrum of MAXI J1348–630 and the spectral-timing properties of the type-B QPO (García et al. 2021). The QPO frequency and spectral state of the source reflect the physical and geometrical properties of the corona. The variability of QPO upon energy and the temperature of the surrounding Comptonizing corona exhibits the same dependence upon QPO frequency in 4U 1636–53 (Karpouzas et al. 2020). The evolution of various physical quantities such as the corona size, temperature and the fraction of the corona photons upon the QPO frequency and spectral state shows a consistent trend in GRS 1915+105 (García et al. 2022) and EXO 1846–031 (Liu et al. 2021), and there is conclusive evidence that the X-ray corona evolved into a jet (Méndez et al. 2022).

In the disk-corona model, the energy of X-ray radiation from the disk and the corona is coupled (Haardt & Maraschi 1993). The reflection to the relatively hard X-ray continuum emission by the optically thick accretion disk shows important features in the spectrum, mainly manifested as three components: the ionized Fe Kα emission lines, the Fe K absorption edge and the Compton reflection hump (Guilbert & Rees 1988; Lightman & White 1988; Fabian et al. 1989). Meanwhile, a broad and asymmetric line profile is produced because of the relativistic effects at several gravitational radii from the central black hole. Fitting these reflection features in the spectrum with suitable reflection models could help us to study the physical mechanism around the black hole (Fabian et al. 1989; Miller 2007; Fabian & Ross 2010).

MAXI J1631–479 is a black hole X-ray binary transient discovered by the Monitor of All-sky X-ray Image (MAXI) on 2018 December 21 (Kobayashi et al. 2018). The spectral properties, state transition and clear changes in the X-ray flux were obtained subsequently (Miyasaka et al. 2018; Negoro et al. 2019; van den Eijnden et al. 2019). The results from the Nuclear Spectroscopic Telescope Array (NuSTAR) observations show evidence for strong relativistic disk reflection features, displaying clear variations in the profile of the broad Fe emission line between the states dominated by disk and power-law; besides, a high black hole spin ($a^{*} > 0.96$) and a low inclination ($i \sim 29^{\circ}$) are estimated (Xu et al. 2020). During the HIMS, type-C QPOs were observed both by the Neutron Star Interior Composition Explorer (NICER) and the Insight-Hard X-ray Modulation Telescope (Insight-HXMT); the centroid frequency of QPOs varies between $\sim$4 and 10 Hz, the QPOs fractional rms remains at $\sim$10% from $\sim$10 keV to $\sim$100 keV, and the hard phase lag for QPOs supports the low inclination BHT (Rout et al. 2021; Bu et al. 2021).

In this work, we study spectral and timing properties of the reflection components of MAXI J1631–479 using data from Insight-HXMT target of opportunity (ToO) observations. In Section 2, we describe the Insight-HXMT observations and data reduction methods. In Section 3, the results are presented. In Sections 4 and 5, we present the discussion and conclusions respectively.

2. Observations and Data Analysis

MAXI J1631–479 was observed by Insight-HXMT from 2019 February 11 (MJD 58525) to 2019 April 9 (MJD 58582). There are 29 observations with a total of 300 ks of exposure time.

Insight-HXMT (Zhang et al. 2020), the first Chinese X-ray astronomy mission, consists of three main payloads: the High Energy X-ray Telescope (HE, 20–250 keV, 5100 cm^2, $\sim$25 μs, Liu et al. 2020), the Medium Energy X-ray Telescope (ME, 5–30 keV, 952 cm^2, $\sim$276 μs, Cao et al. 2020) and the Low Energy X-ray Telescope (LE, 1–15 keV, 384 cm^2, $\sim$1 ms, Chen et al. 2020). The energy resolution is $\sim$17% at 60 keV, $\sim$15% at 20 keV and $\sim$2.5% at 6 keV. The small field of views (FoVs) are $1\overset{\circ}{.}6 \times 6^{\circ}$ for LE, $1^{\circ} \times 4^{\circ}$ for ME and $1\overset{\circ}{.}1 \times 5\overset{\circ}{.}7$ for HE.

2.1. Data Reduction

The Insight-HXMT Data Analysis Software[5] (HXMTDAS) v2.04 and HXMTCALDB v2.04 are used to analyze the data. We filter the data according to the following criteria for good time interval (GTI) selection: (1) elevation angle (ELV) $> 10^{\circ}$; (2) ELV above bright Earth for LE detector $>30^{\circ}$; (3) the value of the geomagnetic cutoff rigidity (COR) > 8 GeV; (4) the offset angle from the pointing direction $<0\overset{\circ}{.}1$; (5) the time before and after the South Atlantic Anomaly passage >100 s. Only small FoVs are selected to avoid possible interference from the bright Earth and local particles.

Light curves of all energy bands are extracted from the screened files using HELCGEN, MELCGEN and LELCGEN tasks with $1/256$ s bins. Spectra are extracted from screened files using HESPECGEN, MESPECGEN and LESPECGEN. In Figure 1, the evolution of the net count rate for the three instruments is depicted in the top three panels and the hardness is displayed in the bottom panel. The count rate for HE instrument of observation P0214003009 (MJD 58536) should be excluded because of its very short GTIs ($<$90 s). In order to study the energy dependence of the type-C QPO frequency in HIMS, six relatively bright Insight-HXMT observations are

[5] http://hxmtweb.ihep.ac.cn/software.jhtml

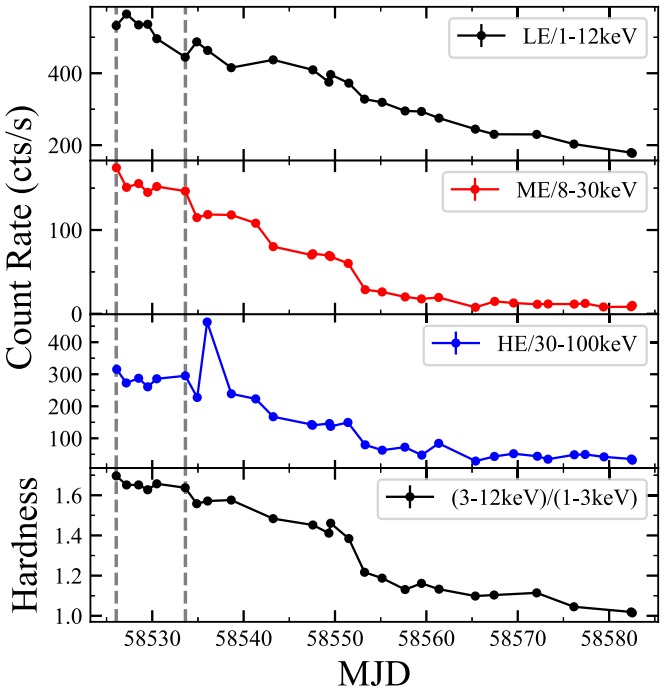

Figure 1. Insight-HXMT light curves and hardness of MAXI J1631–479 of all observations from 2019 February 11 (MJD 58526) to 2019 April 9 (MJD 58582). Hardness is calculated by the ratio of net count rate between the energy bands of 3–12 keV and 1–3 keV for Insight-HXMT/LE data. The observations between the two gray dotted lines are analyzed in this study. Each point corresponds to one exposure. The count rate for the HE instrument of observation P0214003009 (MJD 58536) should be excluded.

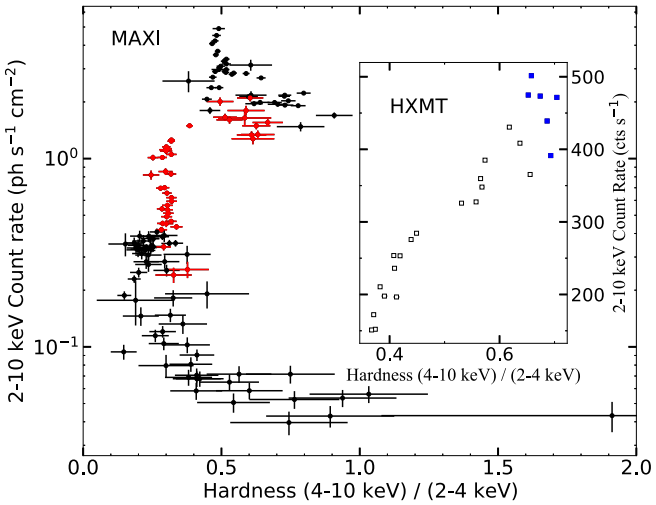

Figure 2. The HID extracted from MAXI data. The hardness is defined between 4–10 keV and 2–4 keV energy bands. The MAXI data points are binned by 1 day, and the red points mark the simultaneous Insight-HXMT observation time. The inset shows the HID extracted from Insight-HXMT/LE data. Each data point represents one Insight-HXMT observation. The blue dots highlight the data used in this study.

selected from MJD 58526 to MJD 58533 between the two gray dotted lines.

In Figure 2, the hardness ratio from MAXI data decreases from ∼1.0 to ∼0.5 during the HIMS according to Bu et al. (2021), and the red points mark the simultaneous Insight-HXMT observation time. MAXI's hardness intensity diagram (HID) is produced with the data from the on-demand web interface.[6] In the inset of Figure 2, the HID from Insight-HXMT is presented, and the data used in this study are marked with blue dots, which have relatively higher count rate and greater hardness.

The background estimations of the three instruments are performed with the Python scripts LEBKGMAP, MEBKGMAP and HEBKGMAP, respectively (Liao et al. 2020a; Guo et al. 2020; Liao et al. 2020b). However, there are several sources, such as GX 340+0, in the field of MAXI J1631–479, whose contamination cannot be estimated with the background software. According to the detailed analysis by Bu et al. (2021), we ignore the background contribution for the data of LE and HE from these sources because of their relatively low count rate. We thus generate the spectra by DetBOXs and discard the events from the contaminated boxes for correcting the spectra for ME correspondingly.

We also use the data of MAXI J1631–479 observed by NICER from 2019 February 11 (MJD 58525) to 2019 February 19 (MJD 58533). A total of nine observations are used in this study. After the event files are downloaded[7], the light curves are generated with the multipurpose tool XSELECT v2.4k[8] with 1/256 s bins.

2.2. Timing Analysis

We produce PDS with a time resolution of 1/64 s from 8 s intervals (Zhou et al. 2021) for each observation using POWSPEC v1.0 (XRONOS v6.0).[9] The PDS is subjected to Miyamoto normalization (Miyamoto et al. 1991) and the Poisson noise component is subtracted (Zhang et al. 1995). The PDS is fitted with two or three Lorentzian functions in XSPEC v12.11.1 (Nowak 2000; Belloni et al. 2002). The reduced chi-squared values of all the best fits are less than 1.5 for the 92 degrees of freedom. Among six observations, the centroid frequency of QPOs varies between 4.8 Hz and 6.2 Hz for the mean PDS, which is shown in Table 1. In addition, the detailed energy dependence of the QPO frequency is analyzed in detail in Section 3.1. We divide the 1–100 keV energy range into six energy bands and produce a PDS for each of them. The six energy bands correspondingly are 1–5 keV (LE), 5.5–7.5 keV

[6] http://maxi.riken.jp/star_data/J1631-478/J1631-478.html

[7] https://heasarc.gsfc.nasa.gov/cgi-bin/W3Browse/w3table.pl

[8] https://heasarc.gsfc.nasa.gov/docs/software/lheasoft/ftools/xselect/

[9] https://heasarc.gsfc.nasa.gov/docs/xanadu/xronos/xronos.html

Table 1
Best-fitting Result of QPO Frequency and its FWHM of MAXI J1631–479 Extracted from Insight-HXMT Data

Obs. ID	Time (MJD)	QPO ν (Hz)	FWHM (Hz)
		LE (1–12 keV)	
P0214003002	58526.1	4.91 ± 0.06	1.0 ± 0.2
P0214003003	58527.2	6.21 ± 0.12	$1.4^{+0.3}_{-0.4}$
P0214003004	58528.5	$5.43^{+0.11}_{-0.10}$	1.5 ± 0.3
P0214003005	58529.5	$6.16^{+0.11}_{-0.12}$	$1.4^{+0.3}_{-0.4}$
P0214003006	58530.5	$5.20^{+0.06}_{-0.05}$	$0.8^{+0.2}_{-0.1}$
P0214003007	58533.6	4.84 ± 0.05	0.8 ± 0.1
		ME (6–38 keV)	
P0214003002	58526.1	5.02 ± 0.05	1.0 ± 0.1
P0214003003	58527.2	6.19 ± 0.03	0.7 ± 0.1
P0214003004	58528.5	5.48 ± 0.04	$1.0^{+0.2}_{-0.1}$
P0214003005	58529.5	6.13 ± 0.03	0.7 ± 0.1
P0214003006	58530.5	5.21 ± 0.02	0.5 ± 0.1
P0214003007	58533.6	4.89 ± 0.02	0.6 ± 0.1
		HE (26–200 keV)	
P0214003002	58526.1	5.33 ± 0.05	0.7 ± 0.1
P0214003003	58527.2	$6.15^{+0.12}_{-0.09}$	$0.9^{+0.3}_{-0.2}$
P0214003004	58528.5	5.43 ± 0.04	$0.8^{+0.2}_{-0.1}$
P0214003005	58529.5	6.17 ± 0.03	0.6 ± 0.1
P0214003006	58530.5	5.21 ± 0.03	0.5 ± 0.1
P0214003007	58533.6	4.86 ± 0.02	0.5 ± 0.1

Note. The errors are calculated with 1σ level uncertainties. The energy bands selected are 1–12 keV (LE), 6–38 keV (ME) and 26–200 keV (HE). In Section 2.2, we describe the details of the PDSs.

(LE), 8–12 keV (ME), 12–20 keV (ME), 20–40 keV (HE) and 40–100 keV (HE). In Figure 3, we show three representative PDSs for 1–5 keV (LE), 5.5–7.5 keV (LE) and 8–12 keV (ME) energy bands.

2.3. Spectral Analysis

We fit the spectra with three different model combinations using XSPEC-v 12.10.1 f. Model (a) is `constant*TBabs*(diskbb+nthComp+Gaussian+Gaussian)`, model (b) is `constant*TBabs*(diskbb+relxilllpCp)` and model (c) is `constant*TBabs*(diskbb +nthComp +relxilllpCp)` in which the constant is used to account for the calibration differences of the effective areas of LE, ME and HE.

In model (a), the free-fitting values of the broad Fe line energy are basically unchanged. It is necessary to note that fitting an Fe line profile with only one `Gaussian` is not enough, as demonstrated in the left panel of Figure 4, where a distinct narrow structure appears. Because the flux of the narrow Fe line evolves significantly, only during MJD 58527.2-58529.5 and on MJD 58533.6 can it be freely fitted well due to the relatively high flux, and its central energy and σ are approximately unchanged. While on MJD 58526.1 and 58530.5, due to the small flux of the narrow Fe line, the insignificant narrow Fe line does not constrain the free-fitting values well. In order to obtain the evolution of the narrow Fe line, on the basis of the unification of variables, the central energy of the two `Gaussians` are frozen at 6.4 keV and 6.7 keV respectively, representing the narrow and broad components of the Fe line correspondingly, and the σ of the narrow Fe line is fixed at 0.2 keV. $kT_{\rm bb}$ (the seed photon temperature) of `nthComp` is linked to $T_{\rm in}$ (the temperature at inner disk radius) of `diskbb`.

In model (b), the fit of some parameters is not sensitive to their exact values, because of the statistical limitation of Insight-HXMT data selected in this study; and they are fixed at reasonable values according to the NuSTAR data studied by Xu et al. (2020). The fixed parameters are as follows: $a^{*}(\mathrm{cJ/GM^2}) = 0.96$, $i(^\circ) = 29$ and $A_{\rm Fe}(\mathrm{solar}) = 1$, because these parameters should be considered unchanged during the whole outburst. The switch of the `relxilllpCp` model is set to 1 which means reflection fraction is interpreted as boost parameter (Dauser et al. 2014; García et al. 2014). The reflection fraction $R_{\rm ref}$ is fixed at 1 and the normalization *norm* is left free. The other two insensitive parameters are fixed, $kT_{\rm e}(\,\mathrm{keV}) = 400$ and $R_{\rm out}(r_{\rm g} \equiv GM/c^2) = 200$.

In model (c), $R_{\rm ref}$ is set to -1, in this case, the `relxilllpCp` only calculates the reflected part, and the direct emission is taken care of by `nthComp`. This is because the default seed photon temperature of `relxilllpCp` is only 0.05 keV, which is much lower than the temperature ($\sim$1 keV) of the disk, and it is not suitable for fitting the direct emission part. Model (c) is more complex than the previous two model combinations, and some parameters that can be constrained in model (b) must be fixed here, otherwise, the data cannot constrain the parameters of model (c) well. From the fit of the same parameters in model (b), the additional fixed parameters are as follows: the radius at inner disk $R_{\rm in} = 12\,r_{\rm g}$ and the height of the primary source above the black hole $h = 5\,r_{\rm g}$. In addition, $kT_{\rm bb}$ of `nthComp` is linked to $T_{\rm in}$ of `diskbb`.

In Figure 4, the spectra of observation P0214003003 with three model combinations are displayed, whose values of reduced chi-squared are 1.09, 1.08 and 1.07 respectively. All the spectral fitting results are shown in Table A1.

3. Results

3.1. Power Density Spectra

For each of the six energy bands described in Section 2.2, the corresponding PDSs are produced. Figure 5 features the QPO centroid frequency as a function of energy from 1 keV to 100 keV, and the data, excluding the second data point (Fe line/ 5.5–7.5 keV), are fitted with a straight line

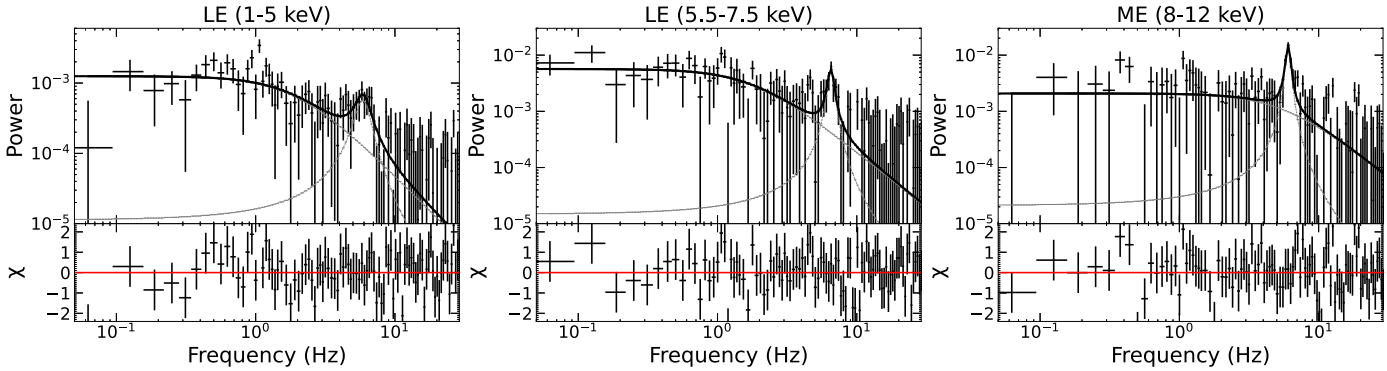

Figure 3. PDSs of Obs. ID P0214003005 (MJD 58529.5) extracted from 1 to 5 keV (LE), 5.5 to 7.5 keV (LE) and 8 to 12 keV (ME). Two Lorentzian functions are applied to fit the PDS. The centroid frequency of QPOs is ∼5.9 Hz (left), ∼6.3 Hz (middle) and ∼6.1 Hz (right). The error bars show 1σ level uncertainties.

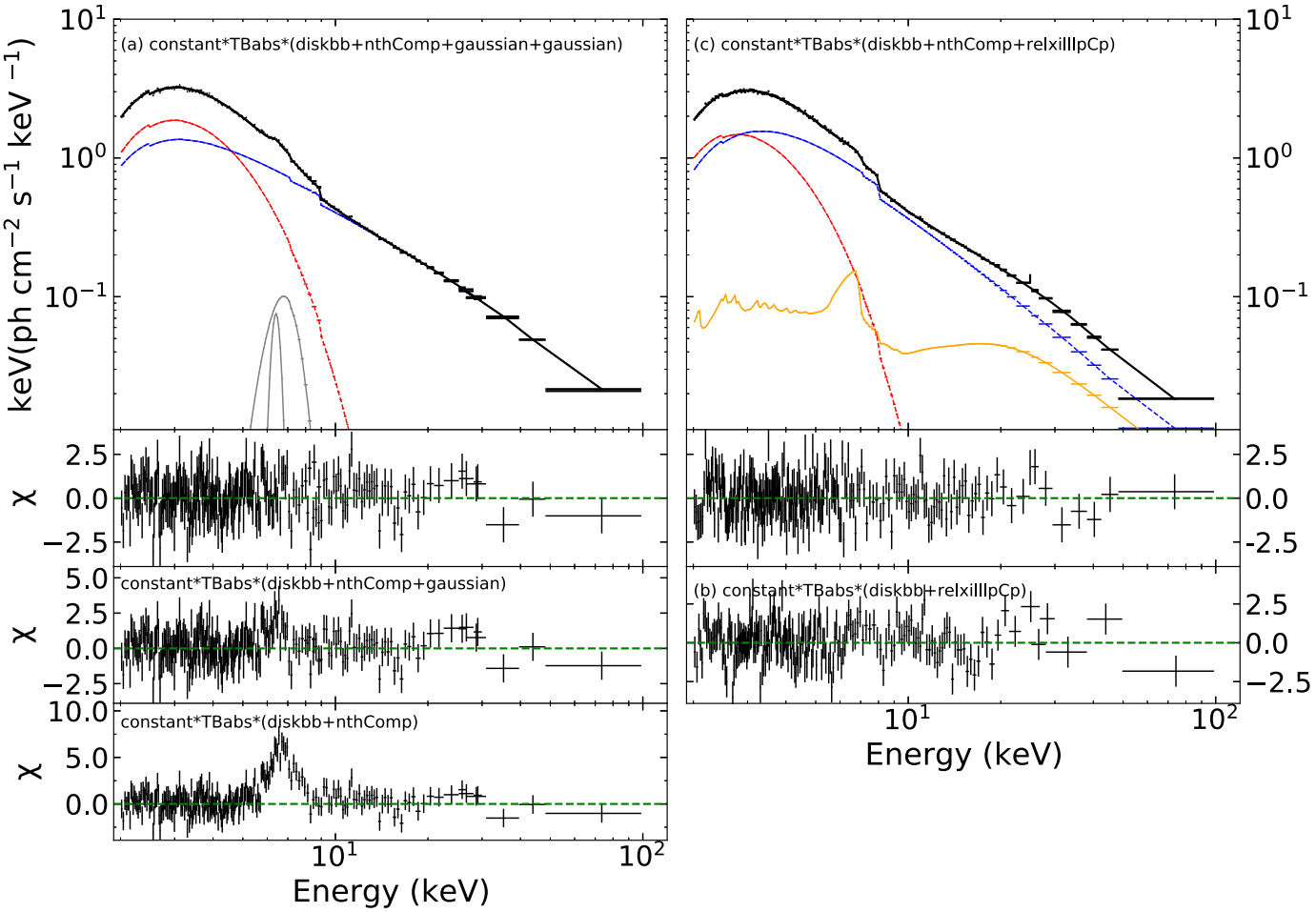

Figure 4. Unfolded Insight-HXMT spectra of MAXI J1631–479 of Obs. ID P0214003003 (MJD 58527.2). (Left) The total model (black line) is plotted together with `diskbb` (red line), `nthComp` (blue line) and two `Gaussians` (gray line). (Right) The total model (black line) is plotted together with `diskbb` (red line), `nthComp` (blue line) and `relxilllpCp` (orange line). The bottom left panel shows the profile of the Fe line. The spectra are rebinned for clarity.

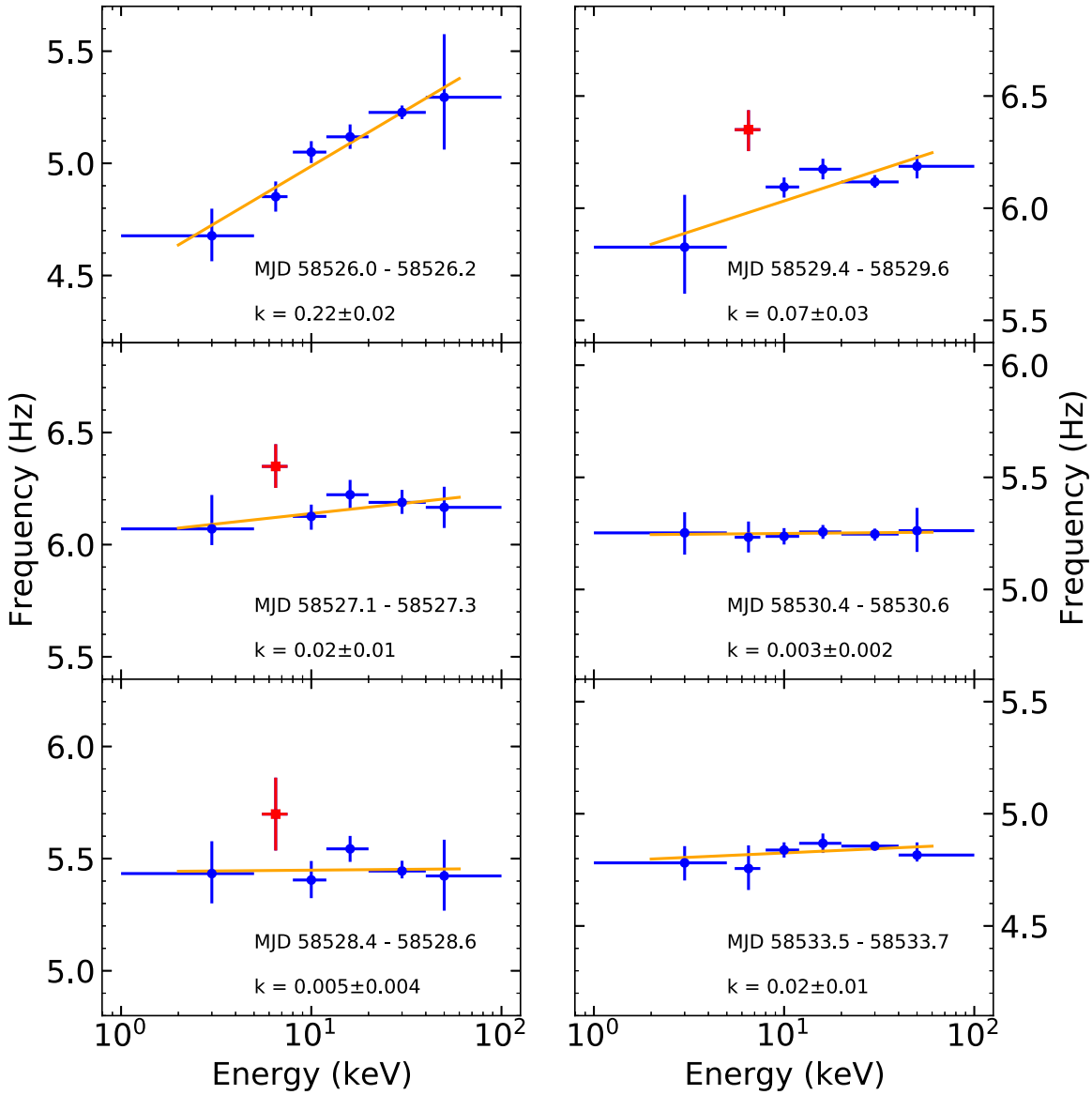

Figure 5. Centroid frequency of type-C QPOs as a function of energy. The constant k is the slope of the orange line. The second data point represents the 5.5–7.5 keV energy band and the red square dots deviate from the overall trend. The errors are calculated with 1σ level uncertainties.

(QPOν(Hz) = k $\cdot$ $\log_{10}$E(keV) + b; k, b = constant). We suggest that the top-left panel (MJD 58526.0—58526.2) displays an increasing trend, and the slope of the fitting line is 0.22 ± 0.02. In the other five panels, the slope of the fitting line is close to zero; the QPO frequency as a function of energy remains approximately constant. The slopes with 1σ error are expressed at the bottom of each panel.

It is worth noticing that, during MJD 58527.1 to MJD 58529.6, the QPO frequency around the Fe line energy range marked with red square dots is higher than that of any other energy band, and this is the phenomenon of Fe line's QPO frequency jump. The average frequency difference calculated by subtracting the orange fitting line from the Fe line's frequency is $\Delta f = 0.25 \pm 0.08$ Hz. Meanwhile, the other three observations do not have this phenomenon of Fe line's QPO frequency jump. However, the significance of Δf is just 3.13σ; in order to check if this phenomenon is significant, we compare the result between the almost simultaneous data of Insight-HXMT and NICER. In Figure 6, the evolutions of QPO frequency observed by both NICER and Insight-HXMT are similar (except for the third Insight-HXMT observation, explained in detail below). During the time indicated by the shaded area, the frequency jump exists in both top and bottom panels; the black dashed line is above all other colored dotted

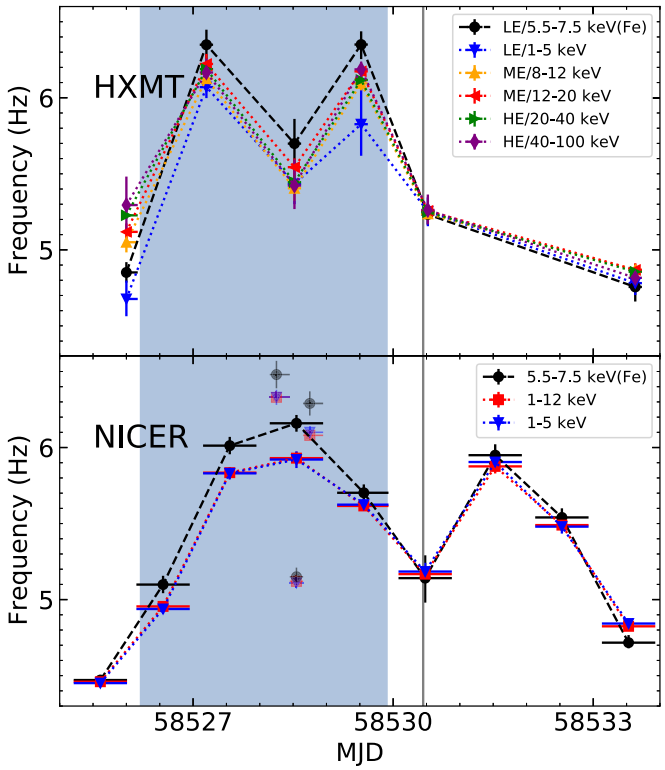

Figure 6. The evolution of centroid frequency of type-C QPOs in Insight-HXMT and NICER data. The different colored lines represent different energy bands labeled in the plot. The shaded area highlights the area with the highest black dashed line (Fe line's QPO frequency jump). The gray solid line marks the overlapping points of all energy bands. Each point represents one observation. The errors are calculated with 1σ level uncertainties.

lines. The NICER observation has a better signal-to-noise ratio (SNR), and it is obvious that the QPO frequency of the Fe line is higher than the other energy bands, with the frequency difference $\Delta f = 0.19 \pm 0.03$ Hz between the Fe line and the 1–5 keV energy band. After the shaded area, about MJD 58530.5 marked by the gray vertical line, the QPO frequencies of all the energy intervals overlap precisely. Moreover in the other white area, the black dashed line is also not above other colored dotted lines. To assess the significance of the possible Fe line's QPO frequency jump, all the PDSs, in all energy bands, are simultaneously fitted with the same model. For Insight-HXMT, set the parameters of all the Lorentzians free in the first PDS, and link the frequencies and full width at half maximum (FWHM) of the Lorentzians in all the other PDSs to those of the first PDS. The FWHMs of FTN at 1-5 keV and 5.5-7.5 keV energy bands are linked, and the FWHMs of FTN at the other four energy bands are linked, because the FTN changes a lot between LE and ME/HE. On MJD 58529.5 (Obs.005), the frequency of simultaneous fitting is 6.13 ± 0.02 Hz, the FWHM is 0.67 ± 0.06 Hz and the χ^2/dof is 625/446. Then, the frequencies of QPO are untied, and the frequencies of the QPO are allowed to be fit freely. In this case, the FWHM is 0.62 ± 0.05 Hz, and the χ^2/dof is 547/441, the QPO frequency is 6.49 ± 0.11 Hz at the 5.5–7.5 keV energy band, and 5.83 ± 0.13 Hz at the 1–5 keV energy band. In addition, although NICER only has low-energy data, we also present the same work for comparison. The FWHM is 1.12 ± 0.07 Hz; the QPO frequencies are 6.25 ± 0.05 Hz at the 5.5–7.5 keV energy band, and 6.07 ± 0.04 Hz at the 1–5 keV energy band. The complete results are presented in Table A2. As shown in Figure 7, the PDSs in all energy bands are fitted with the same model simultaneously for Insight-HXMT and NICER. After keeping all the parameters (except the normalizations) of any other component in the model linked in all fits, only the frequencies of the Lorentzian are free to fit the QPO, and the Fe line's QPO frequency is still higher than that at other energy bands.

In panel (1) of Figure 8, the evolution of the QPO frequency difference shows a similar trend for Insight-HXMT and NICER data; in the shaded area, the QPO frequency difference is greater than zero. For Insight-HXMT data, the QPO frequency difference is calculated by subtracting the fitting line from the Fe line's frequency, and the average frequency difference $\Delta f = 0.25 \pm 0.08$ Hz, which has about 3.13σ significance. For NICER data, the QPO frequency difference is calculated by subtracting the frequency at the 1–5 keV energy band from the Fe line's frequency, and the average frequency difference $\Delta f = 0.19 \pm 0.03$ Hz, which has about 6.33σ significance.

In conclusion, although there is no higher reference energy band for NICER data because of the low count rate in the 7–12 keV band, the consistency in time between Insight-HXMT and NICER data allows us to confirm that the phenomenon of Fe line's QPO frequency jump does exist.

The QPO frequency of all energy bands generally increases first and then decreases with time, and in the period indicated by the shaded area, when the Fe line's QPO frequency jumps, the QPOs have a relatively high centroid frequency. On MJD 58528.5, the inconsistent trend between the third Insight-HXMT point and the fourth NICER point in Figure 6 is caused by the different exposure time range, because the QPO frequency evolves rapidly over time. As shown in the bottom panel of Figure 6, the fourth longer NICER observation is divided into three segments (unconnected discrete points), and the second segment with the same exposure time has the same downward trend in the Insight-HXMT data. The shorter Insight-HXMT observation is exactly in the dip of the light curve of NICER at the red dashed line as displayed in Figure 9.

In Figure 9, there is a small flare in the light curves which is labeled by a gray dashed line for the NICER data, and the Insight-HXMT data also display an increase first, followed by a declining trend at the same position. Marking the period of the Fe line's QPO frequency jump, the shaded area completely covers this small flare.

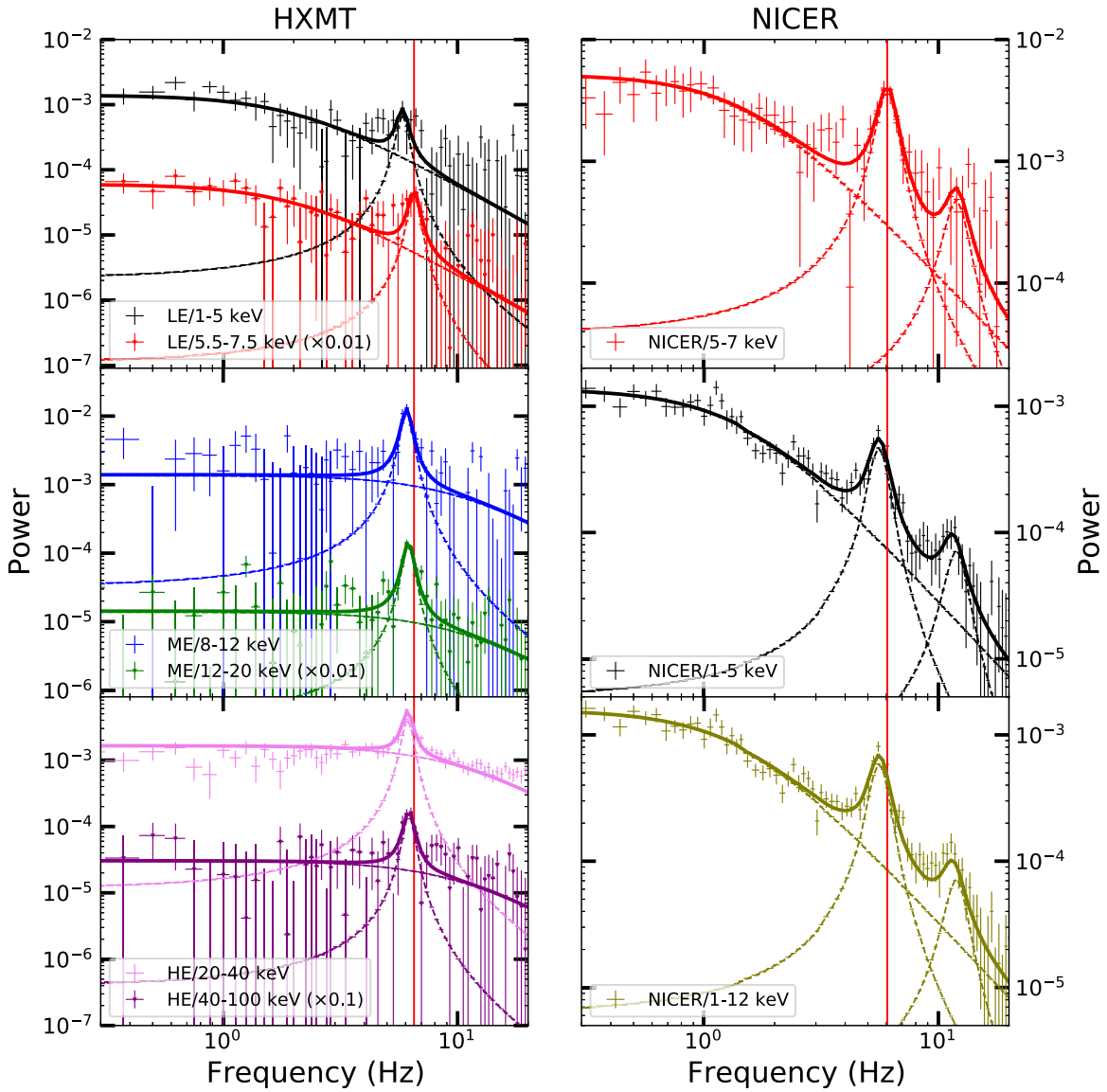

Figure 7. The PDSs in all energy bands are fitted with the same model simultaneously for Insight-HXMT during MJD 58529.4-58529.6 and NICER during MJD 58528.1-58528.9. The FWHM values of the Lorentzians are linked, for Insight-HXMT, the FWHM of the FTN changes a lot between LE and ME/HE, thus the values of FWHM at 1–5 keV and 5.5–7.5 keV energy bands are linked, and the values of FWHM at the other four energy bands are linked, respectively. Different colored lines represent different energy bands. The red vertical line marks the QPO frequency of the Fe line energy band, to the right of the QPO of all other energy bands, meaning that it has the highest QPO frequency. The error bars show 1σ level uncertainties. The complete results are presented in Table A2.

3.2. Iron Line

We fit the spectra extracted from Insight-HXMT observations using model (a). The profile of Fe emission line is fitted with two Gaussian functions as depicted in Figure 4(a); the broad and narrow Gaussian functions represent the broad and narrow components of the Fe line respectively. The fitting results are shown in Table A1.

In Figure 8, panel (3) displays the evolution of the equivalent width (EW) of the narrow Fe line flux. It is obvious that the EW in the period indicated by the shaded area is higher than the others on the whole, and the average difference is 0.0140 ± 0.0037 keV, which has about 3.78σ significance. Thus, the narrow Fe line increases its EW first and then decreases its EW before and after the shaded area. Panel (4) shows the evolution of the EW of the broad Fe line flux, and it remains approximately constant. While the Fe line evolves, the continuum spectrum does not show any obvious evolution related to the Fe line. In brief, in the shaded area, the narrow component of the Fe

line has a higher flux than the overall trend, whereas there is no special change in the broad component of the Fe line.

3.3. Spectra

As plotted in Figure 4, we use the `relxilllpCp` model to fit the reflection spectra, and get more important spectral parameters such as the height of corona and the inner disk radius. In Table A1, we express the best-fitting results of models (b) and (c).

In Figure 8, panels (5) and (6) show the evolution of the radius at inner disk $R_{\rm in}$ and the primary point source above the black hole h of `relxilllpCp` in model (b), respectively. They are considered to remain constant more or less, because the difference between their maximum and minimum values is only $5.0 \pm 3.2\ r_{\rm g}$ ($R_{\rm in}$) and $2.0 \pm 1.4\ r_{\rm g}$ (h), whose significance of deviation is only 1.56σ and 1.43σ respectively.

Panel (2) shows the evolution of *norm* of `relxilllpCp` in model (c), where this *norm* only represents the normalization of the reflected part. The points marked with red in the shaded area are approximately higher than the others, and on the whole, the average difference is $2.03^{+0.75}_{-0.88}(\times 10^{-2})$, which has about 2.31σ significance. The larger errors are hard to avoid because of the complexity of model (c) and the limitation of data. Due to the lower significance of deviation, we consider that there is only a marginally increasing trend in the shaded area.

4. Discussions

We have reported the energy dependence of the type-C QPO frequency in HIMS of the BHT MAXI J1631–479 using Insight-HXMT and NICER data. For the first time, we discover that the QPO frequency around the Fe line energy range is higher than that of any other energy band when a small flare occurred, which has never been observed for all other BHTs. The QPO frequency as a function of energy displays an increasing trend first (MJD 58526.0-58526.2) and then remains constant (MJD 58527.1-58533.7) as depicted in Figure 5. The QPO frequency of all energy bands generally increases first and then decreases with time as illustrated in Figure 6. During this flare, the flux of the narrow Fe line increases while the broad Fe line remains constant. The spectral fitting results also support that the normalization of the reflected part marginally increases, and both the inner disk radius and the height of the primary point source remain constant, approximately (Figure 8). As affirmed in Figures 10 and 11, there is a significant positive correlation between the QPO frequency and the EW of the narrow Fe line, and the QPO frequency and the count rate.

The variations in the narrow Fe line detected in the hard state of GX 339-4 (Tomsick et al. 2009) and MAXI J1820+070 (Kara et al. 2019; You et al. 2021; Wang et al. 2021; Mao et al. 2022) are related to the line emission region at a large distance (Oosterbroek et al. 1996; King et al. 2015), based on the

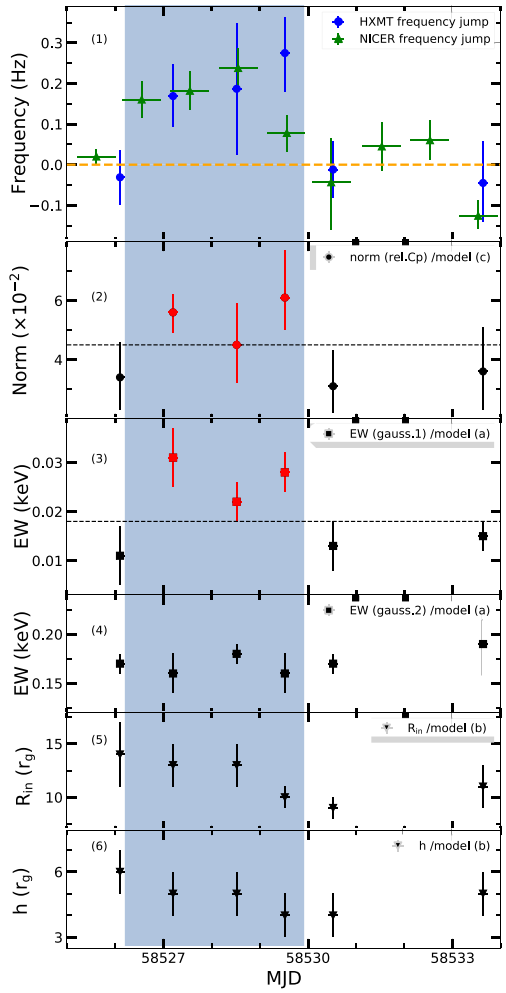

Figure 8. Evolution of QPO frequency difference and some spectral parameters with time. Panel (1): The evolution of the QPO frequency difference. For Insight-HXMT data, the QPO frequency difference is calculated by subtracting the fitting line from the Fe line's frequency, and the average frequency difference in the shaded area, $\Delta f = 0.25 \pm 0.08$ Hz. For NICER data, the QPO frequency difference is calculated by subtracting the frequency at 1–5 keV energy band from the Fe line's frequency, and the average frequency difference $\Delta f = 0.19 \pm 0.03$ Hz. Panel (2): The *norm* of the `relxilllpCp` in model (c). In the shaded area, the points marked with red are higher than other points. Panel (3): The EW of the first `Gaussian` in model (a), which represents the flux of the narrow Fe line. In the shaded area, the points marked with red are higher than other points, and the average difference is 0.0140 ± 0.0037 keV. Panel (4): The EW of the second `Gaussian` in model (a), which represents the flux of the broad Fe line. Panel (5): The radius at inner disk, $R_{\rm in}(r_{\rm g})$, of the `relxilllpCp` in model (b). Panel (6): The height of the point source, $h(r_{\rm g})$, of the `relxilllpCp` in model (b).

sufficiently narrow and symmetric profile. Fe emission includes a prominent broadened line due to He-like Fe at 6.7 keV (Koyama et al. 1986; Kaneda et al. 1997; Revnivtsev et al. 2009). The variation of the relativistically broadened Fe emission line reflects the change in the inner accretion disk radius in a black hole X-ray binary (Xu et al. 2020). The narrow Fe line superimposed on top of the broad Fe emission

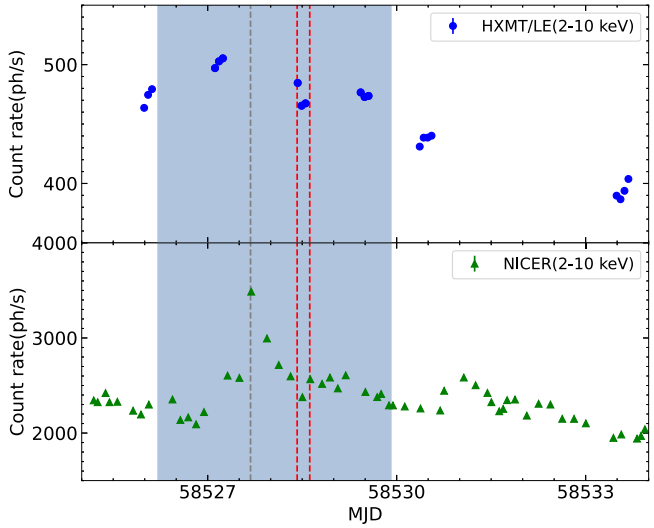

Figure 9. The Insight-HXMT/LE (2–10 keV) and NICER (2–10 keV) light curves. Each point represents 1.5 hr. The shaded area corresponds to the period of the Fe line's QPO frequency jump. The gray dotted line marks the peak of the flare. The red dotted lines signify that the shorter Insight-HXMT observation is exactly in the dip of the light curve of NICER.

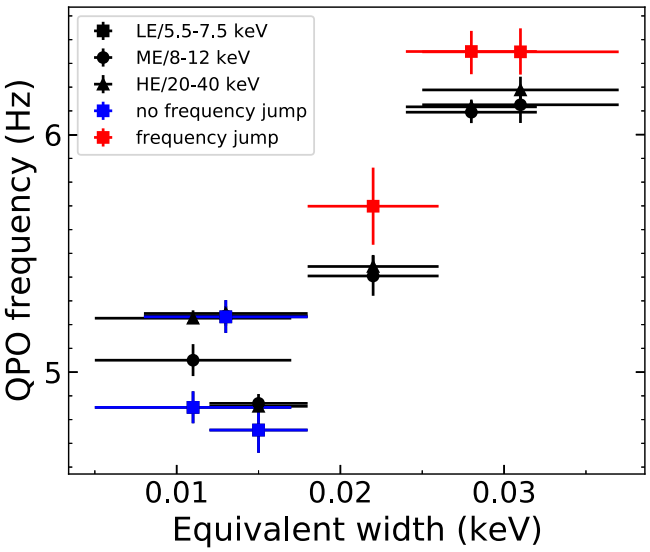

Figure 10. The relation between the QPO frequency and the parameter *norm* in *Gaussian* of the narrow component of Fe line. The points with different shapes represent different energy bands labeled in the plot.

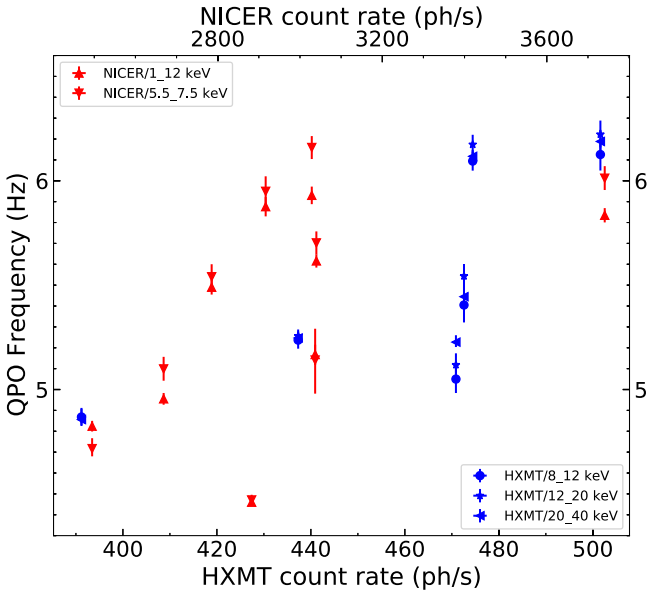

Figure 11. The relation between the QPO frequency and the count rate. The different colored points of different shapes labeled in the plot represent different energy bands. The count rates for Insight-HXMT (bottom) and NICER (top) use different horizontal axes.

line profile also supports the existence of different reflection regions (Walton et al. 2017; Xu et al. 2018; Miller et al. 2018; Jana et al. 2021).

The energy dependence of QPO fractional rms and time lag for MAXI J1631–479 support the LT precession of the jet model (Bu et al. 2021); the QPO time-lags generally exhibit hard lags for the whole energy band with ∼4 ms, and the rms increases with photon energy from 1 keV to ∼10 keV and remains more or less constant from ∼10 keV to ∼100 keV, which is inconsistent with the prediction of the hot inner flow model at a low inclination angle (You et al. 2018), while the jet model could explain these results. The corona in the lamppost geometry could be interpreted as a standing shock through which the material flows (You et al. 2021). We thus suggest that the corona in MAXI J1631–479 is also jet-like. We obtained the Insight-HXMT spectra of MAXI J1631–479 and find that the broad and narrow Fe emission line is variable in line strength and width with short timescale. The narrow

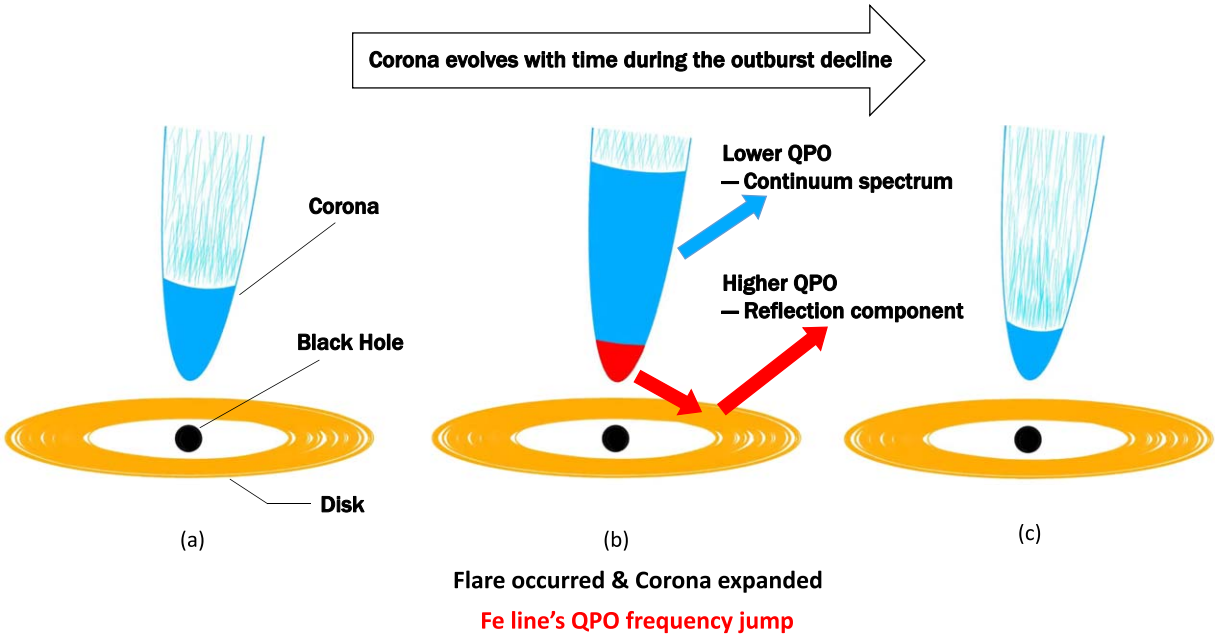

Figure 12. The schematic of the jet-like corona in the HIMS. The hard photons from the corona illuminate the disk, resulting in the reflection component. When the corona contracts toward the black hole normally during the outburst decline, an unexpected small flare occurred, accompanied by the corona expansion. The expanded corona appears approximately in layers, hence the higher QPO frequency of the reflection component is observed. At stage (a), the inner-jet precession closest to the black hole is faster than the outer-jet, causing a higher QPO frequency at inner-parts than outer-parts, thus the QPO frequency as a function of energy has a positive correlation. At stage (b), the corona expanded and a flare occurred, then the large-scale corona was layered; the radiation from the outer corona is rarely reflected by the disk while the inner corona is mainly reflected by the disk. The outer corona is far away from the black hole, thus it has a lower precession frequency. The inner corona is closest to the black hole, thus it has the highest precession frequency; the observed QPO at 5.5–7.5 keV energy band is mainly contributed by the inner corona with a higher QPO frequency. The QPOs at other energy bands are mainly contributed by the outer corona with lower QPO frequency. The phenomenon of Fe line's QPO frequency jump can be explained this way. At stage (c), the corona contracted back to normal scale, and it is smaller than at stage (a), where the energy dependence of QPO frequency remains constant because of the lack of differential precession.

component of the Fe line increases first and then decreases (depicted in Figure 8), while the broad Fe line shows little or no increase. As previously studied on MAXI J1820+070 by Kara et al. (2019), in addition to the unchanging broad Fe line, the EW of a narrow component decreases with time; this decrease is due to the collapse of a vertically extended corona. Meanwhile, there is little or no evolution in the truncation radius of the inner disk during the hard state. In this study on MAXI J1631–479, the EW of the narrow component increases during the flare, while the broad Fe line and the truncation radius of the inner disk remain constant. The normalization of the reflected part also increases during this flare. Compared to their study, an inverse process (expansion, the opposite of collapse of MAXI J1820+070) of corona evolution of MAXI J1820+070 could explain the results of MAXI J1631–479.

If this evolution of Fe line is related to the vertically extended corona, as the corona expands first, the solid angle of illumination for the disk at the top of the corona (large radii) increases, thus the narrow Fe line increases its EW first when the flare starts (see Section 3.2). Then, as the corona contracts, the solid angle of illumination for the disk at the top of the corona decreases, thus the narrow Fe line decreases its EW when the flare ends. We thus suggest that this small flare might be related to the expansion of the corona.

The profile of the relativistically broadened Fe line remains constant (see panel (4) of Figure 8), which reflects no change in the inner radius of the accretion disk. The spectral results also show that the truncation radius of the inner disk remains constant during coronal expansion, and the height of the corona also remains constant (see Section 3.3). The small deviations between maximum and minimum values of both the truncation radius and the height of the corona are less than 1.6σ, hence the inner disk radius and the height of the corona are considered to remain constant in our jet-like corona model.

In Figure 12, three stages of the jet-like corona evolution are illustrated in schematic. At the early stage, the medium size corona was above the black hole. At the medium stage, a small flare occurred, accompanied by expansion of the corona in the vertical direction. At the final stage, the flare was over, accompanied by the corona contraction again, and the corona became smaller than at the early stage.

The jet radiates photons of different energies at different positions in the radial direction, and differential precession of the jet results in different QPO frequencies. Thus, at the early

stage, the energy dependence of QPO frequency could be caused by differential precession of the vertically extended jet. It is assumed that a jet closer to the black hole produces higher energy radiation. The inner-jet precession closest to the black hole is faster than that of the outer-jet, causing a higher QPO frequency at inner-parts than outer-parts. In this model, the QPO frequency as a function of energy has a positive correlation as affirmed in Figure 5 (MJD 58526.0-58526.2). When this differential precession of the vertically extended jet is not obvious, the QPO frequency as a function of energy remains constant as shown in Figure 5 (MJD 58530.5 and 58533.6).

During the small flare, when the corona expands, the QPO frequency of 5.5–7.5 keV energy band jumps above the overall trend. This jump may be related to the evolution of the reflection component, and as demonstrated in Figure 10, there is a significant positive correlation between the QPO frequency and the EW of the narrow Fe line. The Fe's line frequency jump exists in a period when both the QPO frequency and the EW of the narrow Fe line are higher (red square points). As discussed above, we consider that this evolution of the narrow Fe line represents the coronal evolution. As the corona expands, the large-scale corona is layered; the large size in the vertical direction leads to significant differences in reflectivity. The radiation from the outer corona is rarely reflected by the disk while the inner corona is mainly reflected by the disk. Due to differential precession of the vertically extended jet, the outer corona is far away from the black hole, and it has lower precession frequency; the inner corona is closest to the black hole, and it has the highest precession frequency. An Fe Kα line is emitted from the relativistic accretion disk which is irradiated by the jet. The QPO of the reflection component originates from the precession of the jet. Due to the inclination of the disk, Doppler boosting causes modulation of the illumination flux on the disk from the jet. The asymmetric illumination pattern of the precessing jet on the disk naturally results in the modulation of the reflection component (including the Fe line) with the same frequency, since the observed reflection component of the inner accretion disk is also intrinsically asymmetric. In this mechanism, the observed QPO at the 5.5–7.5 keV energy band is mainly contributed by the inner corona with higher QPO frequency, and the QPOs at other energy bands are mainly contributed by the outer corona with lower QPO frequency. The phenomenon of the Fe line's QPO frequency jump could also be explained. In addition to the reflection component, the inner corona also contributes to the highest energy part of the continuum. At the end of the flare, the corona contracts back to the normal scale. The QPO phase lag is important for this model, but significant results are not obtained because of the large errors.

The evolution of QPO frequency is related to their accretion rate as demonstrated in Figure 11, where a higher accretion rate generally leads to a higher QPO frequency. This mechanism may be related to the speed of the jet. For a vertically distributed corona with a constant radius, we assume a relationship between QPO frequency and precession speed

$$f(E) = K \cdot \beta_{\varphi}(E) \cdot \cos\theta + \mathrm{B} = \mathrm{K} \cdot \cos\theta \cdot \omega(\mathrm{E}) \cdot \mathrm{r} + \mathrm{B}, \quad (1)$$

where K is positive constant, B is constant, $\beta_{\varphi}(E)$ is the projected speed of the jet with respect to the xy-plane (z-axis is aligned with the BH spin), θ is the projected angle to the line-of-sight, $\omega(E)$ is the angular velocity of precession, r is the radius of the jet and E is energy. The QPO frequency $f(E)$ varies with energy, meaning the change of $\omega(E)$. The observed QPO frequency decreases with decreasing energy, suggesting that the speed of the jet decreases. As the jet moves away from the black hole, the energy of photons radiated by the jet decreases and the speed of jet also decreases accordingly. Therefore, there is deceleration in the jet, which may be caused by the magnetic field, whose specific mechanisms need further study. You et al. (2021) discovered that the corona outflows faster as it contracts toward the black hole, suggesting the speed of jet evolves with time. It could be used to explain that the evolution of QPO frequency in time could be caused by the evolution of the speed of the jet. Ma et al. (2021) proposed a jet model to describe the origin of type-C QPOs. LFQPOs at different energies are produced from different parts of the jet with the same frequency. However, different from MAXI J1820+070, the variable energy dependence of QPO frequency for MAXI J1631–479 supports that the energy dependence of the speed of a jet should be considered. To understand the physical mechanism of the speed of the jet, more and better observations are needed.

As described above, this possible new phenomenon of the Fe line's QPO frequency jump has only 3.13σ significance which is not enough for a significant claim. Meanwhile, the rapid evolution of a QPO over time makes the evaluation of this phenomenon more complex; we cannot rule out the possibility that this QPO moving may cause this phenomenon. Regrettably, the dynamical PDS is not obtained, which is very important to confirm this phenomenon. However, this possible phenomenon of the Fe line's QPO frequency jump is still very interesting, which is meaningful for understanding the origin of type-C QPOs, the disk-corona structure, the reflection mechanism, etc. We expect more and better observations to help us assess this QPO frequency jump, and we also expect that this phenomenon would be discovered in other BHTs.

5. Conclusions

In this work, we present the spectral and timing study of the BHT MAXI J1631–479 during its 2019 outburst using observations from Insight-HXMT and NICER. The main results are as follows:

1. We discovered a possible new phenomenon of Fe line's QPO frequency jump for the first time and explained this phenomenon with a layered jet-like corona.

2. The energy dependence of the type-C QPO frequency in HIMS evolves from a positive correlation to no correlation. We suggest that it is caused by the differential precession of the vertically extended jet.
3. The evolution of QPO frequency is positively related to the narrow component of Fe line and the accretion rate. We infer that the QPO originating from the jet is related to the evolution of the coronal size and speed of the jet, meanwhile, deceleration in the jet is needed to explain the energy dependence of QPO.

Acknowledgments

We are grateful for the anonymous referee's helpful suggestions and comments. This work has made use of data from the Insight-HXMT mission, a project funded by China National Space Administration (CNSA) and the Chinese Academy of Sciences (CAS), and data and software provided by the High Energy Astrophysics Science Archive Research Center (HEASARC), a service of the Astrophysics Science Division at NASA/GSFC. This work has also made use of the MAXI data provided by RIKEN, JAXA and the MAXI team. This work is supported by the National Key R&D Program of China (2021YFA0718500) and National Natural Science Foundation of China (NSFC, Grant Nos. U1838201, U1838202, 11733009, 11673023, U1838111, U1838108, U1838105, U1938102, U2038104, U1838110, U1838113, U1838115 and U2031205).

Appendix
Detailed Fitting Results of Spectra and PDS

Table A1
Spectral Fitting Results of MAXI J1631–479 from Insight-HXMT

Model (a):constantTBabs(diskbb+nthComp+Gaussian+Gaussian)						
Parameter	Obs.002	Obs.003	Obs.004	Obs.005	Obs.006	Obs.007
$N_{\rm H,TBabs}(\times 10^{22})$	3.23 ± 0.03	3.22 ± 0.04	3.23 ± 0.05	3.21 ± 0.04	3.15 ± 0.06	3.17 ± 0.05
$kT_{\rm in}$(keV)	0.99 ± 0.01	1.05 ± 0.01	1.01 ± 0.01	1.03 ± 0.01	1.02 ± 0.01	1.01 ± 0.01
$\rm norm_{(diskbb)}$	1189^{+64}_{-60}	1161^{+59}_{-55}	1306^{+61}_{-57}	1370^{+59}_{-54}	1156^{+45}_{-44}	1190^{+44}_{-42}
Γ	2.26 ± 0.01	2.23 ± 0.02	2.25 ± 0.01	2.22 ± 0.01	2.17 ± 0.01	2.21 ± 0.01
$kT_{\rm e}$(keV)	40^{+4}_{-3}	29 ± 3	32 ± 3	26 ± 1	28 ± 1	31 ± 2
$\rm norm_{(nthComp)}$	2.71 ± 0.08	2.20 ± 0.07	2.37 ± 0.07	2.02 ± 0.06	2.03 ± 0.06	2.11 ± 0.05
$\rm norm_{gauss.1}(\times 10^{-3})$	2.2 ± 1.4	$6.4^{+1.6}_{-1.5}$	4.3 ± 1.2	5.8 ± 1.1	2.8 ± 1.1	3.2 ± 0.8
$Sigma_{\rm gauss.2}$(keV)	0.7 ± 0.1	0.7 ± 0.1	0.8 ± 0.1	0.8 ± 0.1	0.8 ± 0.1	0.8 ± 0.04
$\rm norm_{gauss.2}(\times 10^{-2})$	3.1 ± 0.3	2.9 ± 0.4	3.1 ± 0.3	2.8 ± 0.3	3.0 ± 0.3	3.6 ± 0.4
$\rm factor_{(ME)}$	0.84 ± 0.01	0.86 ± 0.01	0.84 ± 0.01	0.86 ± 0.01	0.84 ± 0.01	0.87 ± 0.01
$\rm factor_{(HE)}$	0.81 ± 0.01	0.85 ± 0.01	0.84 ± 0.01	0.84 ± 0.01	0.80 ± 0.01	0.89 ± 0.01
EW[1](keV, gauss.1)	0.011 ± 0.006	0.031 ± 0.006	0.022 ± 0.004	0.028 ± 0.004	0.013 ± 0.005	0.015 ± 0.003
EW(keV, gauss.2)	0.17 ± 0.01	0.16 ± 0.02	0.18 ± 0.01	0.16 ± 0.02	0.17 ± 0.01	0.19 ± 0.03
χ^2/ν	1.01	1.09	1.06	0.99	1.05	1.08
Model (b):constantTBabs(diskbb+relxilllpCp)						
Parameter	Obs.002	Obs.003	Obs.004	Obs.005	Obs.006	Obs.007
$N_{\rm H,TBabs}(\times 10^{22})$	3.57 ± 0.05	3.54 ± 0.05	3.51 ± 0.04	3.51 ± 0.04	3.33 ± 0.06	3.42 ± 0.05
$kT_{\rm in}$(keV)	0.92 ± 0.01	0.99 ± 0.01	0.98 ± 0.01	0.98 ± 0.01	1.01 ± 0.01	0.93 ± 0.01
$\rm norm_{(diskbb)}$	1142^{+94}_{-71}	1180^{+80}_{-69}	1032^{+88}_{-79}	1145^{+77}_{-60}	1061^{+61}_{-56}	967^{+79}_{-71}
$R_{\rm in}(r_{\rm g} \equiv GM/c^2)$	14 ± 3	13 ± 2	13 ± 2	10 ± 1	9 ± 1	11 ± 2
$h(r_{\rm g})$	6 ± 1	5 ± 1	5 ± 1	4 ± 1	4 ± 1	5 ± 1
Γ	2.35 ± 0.01	2.39 ± 0.01	2.38 ± 0.01	2.40 ± 0.01	2.39 ± 0.01	2.41 ± 0.01
$\log(\xi)$	3.8 ± 0.1	3.4 ± 0.2	3.1 ± 0.1	3.2 ± 0.2	$3.0^{+0.2}_{-0.1}$	3.3 ± 0.1
$\rm norm_{(rel.Cp)}$	0.4 ± 0.1	0.4 ± 0.1	0.5 ± 0.1	0.5 ± 0.1	0.5 ± 0.1	0.4 ± 0.1
$\rm factor_{(ME)}$	0.82 ± 0.01	0.81 ± 0.01	0.82 ± 0.01	0.80 ± 0.01	0.81 ± 0.01	0.82 ± 0.01
$\rm factor_{(HE)}$	0.81 ± 0.01	0.86 ± 0.01	0.85 ± 0.01	0.85 ± 0.01	0.80 ± 0.01	0.83 ± 0.01
χ^2/ν	0.98	1.08	1.03	0.98	0.96	1.08
Model (c):constantTBabs(diskbb+nthcomp+relxilllpCp)						
Parameter	Obs.002	Obs.003	Obs.004	Obs.005	Obs.006	Obs.007
$N_{\rm H,TBabs}(\times 10^{22})$	3.07 ± 0.07	3.10 ± 0.06	3.04 ± 0.06	3.06 ± 0.05	3.01 ± 0.05	3.03 ± 0.06
$kT_{\rm in}$(keV)	0.87 ± 0.02	$0.89^{+0.02}_{-0.01}$	0.88 ± 0.01	0.91 ± 0.02	0.91 ± 0.02	0.88 ± 0.02

Table A1
(Continued)

Model (a):constantTBabs(diskbb+nthComp+Gaussian+Gaussian)						
$norm_{(diskbb)}$	1563^{+171}_{-160}	1712^{+124}_{-99}	1700^{+144}_{-121}	1653^{+110}_{-100}	1426^{+115}_{-84}	1513^{+173}_{-117}
Γ	2.42 ± 0.05	2.52 ± 0.05	2.57 ± 0.04	$2.61^{+0.05}_{-0.06}$	2.45 ± 0.03	2.59 ± 0.02
$norm_{(nthComp)}$	3.8 ± 0.2	4.5 ± 0.4	4.1 ± 0.4	3.8 ± 0.3	3.7 ± 0.3	4.0 ± 0.4
$log(\xi)$	3.3 ± 0.4	2.8 ± 0.1	3.0 ± 0.2	2.8 ± 0.2	2.9 ± 0.1	2.7 ± 0.1
norm(rel. Cp, $\times 10^{-2}$)	$3.4^{+1.2}_{-1.1}$	$5.6^{+0.6}_{-0.7}$	$4.5^{+1.4}_{-1.3}$	$6.1^{+1.6}_{-1.1}$	$3.1^{+1.2}_{-0.9}$	$3.6^{+1.5}_{-1.3}$
$factor_{(ME)}$	0.80 ± 0.01	0.83 ± 0.01	0.81 ± 0.01	0.80 ± 0.1	0.79 ± 0.01	0.80 ± 0.01
$factor_{(HE)}$	0.82 ± 0.01	0.81 ± 0.02	0.82 ± 0.01	0.84 ± 0.2	0.82 ± 0.01	0.81 ± 0.01
χ^2/ν	0.97	1.07	1.04	0.98	1.01	1.04

Notes. The energy bands selected for study are 2–8 keV for LE, 8–30 keV for ME and 25–100 keV for HE. Other frozen parameters are given in Section 2.3.
[a] Equivalent Width.

Table A2
The Best Simultaneous Fitting Result of PDS Extracted from Insight-HXMT Data During MJD 58529.4-58529.6 and NICER Data During MJD 58528.1-58528.9

	NICER			Insight-HXMT					
Energy	Fe	1–5	1–12	Fe	1–5	8–12	12–20	20–40	40–100
freq. $_1$		0[a]				0[b]			
$FWHM_1$		3.8 ± 0.1[b]			4.1 ± 0.5[b]			20.1 ± 2.3[b]	
$norm_1$	1.72 ± 0.01	0.41 ± 0.01	0.48 ± 0.01	1.9 ± 0.2	0.4 ± 0.04	2.1 ± 0.4	2.2 ± 0.4	2.6 ± 0.1	0.5 ± 0.1
freq. $_2$	6.25 ± 0.05	6.07 ± 0.04	6.09 ± 0.03	6.49 ± 0.11	5.83 ± 0.13	6.06 ± 0.04	6.17 ± 0.04	6.12 ± 0.02	6.19 ± 0.06
$FWHM_2$		1.12 ± 0.07[b]				0.62 ± 0.05[b]			
$norm_2$	9.07 ± 0.77	0.93 ± 0.06	1.26 ± 0.06	4.2 ± 0.9	0.7 ± 0.1	11.7 ± 1.3	14.1 ± 1.4	4.4 ± 0.3	1.5 ± 0.2
freq. $_3$		12.4 ± 0.1[b]							
$FWHM_3$		2.4 ± 0.2[b]						…	
$norm_3$	5.8[a]	3.4 ± 0.5	3.8 ± 0.4						

Notes. Serial numbers 1, 2 and 3 represent FTN, QPO and QPO harmonic respectively. For the result of NICER, the FWHM values of Lorentzians in three energy bands are linked. For the result of Insight-HXMT, the FWHM values of Lorentzians at 1–5 keV and 5.5–7.5 keV (Fe) energy bands are linked, and the FWHM values at the other four energy bands are linked. Due to data quality limitations, the QPO harmonic is not obvious, so the third Lorentzian is not required. The errors are given at the 1σ level uncertainties. The freq.2 (QPO frequency) at 5.5–7.5 keV energy band is higher than that of all the other energy bands. Units: energy (keV), freq. $_{1,2,3}$(Hz), $FWHM_{1,2,3}$(Hz), $norm_1(\times 10^{-2})$, $norm_2(\times 10^{-3})$ and $norm_3(\times 10^{-4})$.
[a] Fixed parameters.
[b] Linked parameters.

ORCID iDs

L. M. Song https://orcid.org/0000-0003-0274-3396
Y. L. Tuo https://orcid.org/0000-0003-3127-0110

References

Belloni, T., Homan, J., Casella, P., et al. 2005, A&A, 440, 207
Belloni, T. M. 2010, in States and Transitions in Black Hole Binaries, ed. T. Belloni, Vol. 794 (Berlin: Springer), 53
Belloni, T. M., & Motta, S. E. 2016, in Transient Black Hole Binaries, ed. C. Bambi, Vol. 440 (Berlin: Springer), 61
Belloni, T. M., Motta, S. E., & Muñoz-Darias, T. 2011, BASI, 39, 409
Belloni, T., Psaltis, D., & van der Klis, M. 2002, ApJ, 572, 392
Bu, Q. C., Zhang, S. N., Santangelo, A., et al. 2021, ApJ, 919, 92
Cabanac, C., Henri, G., Petrucci, P.-O., et al. 2010, MNRAS, 404, 738
Cao, X., Jiang, W., Meng, B., et al. 2020, SCPMA, 63, 249504
Casella, P., Belloni, T., & Stella, L. 2005, ApJ, 629, 403
Chen, Y., Cui, W., Li, W., et al. 2020, SCPMA, 63, 249505
Dauser, T., Garcia, J., Parker, M. L., Fabian, A. C., & Wilms, J. 2014, MNRAS, 444, L100
Done, C., Gierliński, M., & Kubota, A. 2007, A&ARv, 15, 1
Fabian, A. C., Rees, M. J., Stella, L., & White, N. E. 1989, MNRAS, 238, 729
Fabian, A. C., & Ross, R. R. 2010, SSRv, 157, 167
Fender, R. P., Homan, J., & Belloni, T. M. 2009, MNRAS, 396, 1370
García, F., Karpouzas, K., Méndez, M., et al. 2022, MNRAS, 513, 4196
García, F., Méndez, M., Karpouzas, K., et al. 2021, MNRAS, 501, 3173
García, J., Dauser, T., Lohfink, A., et al. 2014, ApJ, 782, 76
Gilfanov, M. 2010, in X-Ray Emission from Black-Hole Binaries, ed. T. Belloni, Vol. 794 (Berlin: Springer), 17
Guilbert, P. W., & Rees, M. J. 1988, MNRAS, 233, 475
Guo, C.-C., Liao, J.-Y., Zhang, S., et al. 2020, JHEAp, 27, 44

Haardt, F., & Maraschi, L. 1993, ApJ, 413, 507
Homan, J., Bright, J., Motta, S. E., et al. 2020, ApJ, 891, L29
Ingram, A., Done, C., & Fragile, P. C. 2009, MNRAS, 397, L101
Jana, A., Jaisawal, G. K., Naik, S., et al. 2021, RAA, 21, 125
Kaneda, H., Makishima, K., Yamauchi, S., et al. 1997, ApJ, 491, 638
Kara, E., Steiner, J. F., Fabian, A. C., et al. 2019, Natur, 565, 198
Karpouzas, K., Méndez, M., Ribeiro, E. M., et al. 2020, MNRAS, 492, 1399
King, A. L., Miller, J. M., Raymond, J., Reynolds, M. T., & Morningstar, W. 2015, ApJL, 813, L37
Kobayashi, K., Maruyama, W., Negoro, H., et al. 2018, ATel, 12320, 1
Koyama, K., Makishima, K., Tanaka, Y., & Tsunemi, H. 1986, PASJ, 38, 121
Liao, J.-Y., Zhang, S., Lu, X.-F., et al. 2020a, JHEAp, 27, 14
Liao, J.-Y., Zhang, S., Chen, Y., et al. 2020b, JHEAp, 27, 24
Lightman, A. P., & White, T. R. 1988, ApJ, 335, 57
Liu, C., Zhang, Y., Li, X., et al. 2020, SCPMA, 63, 249503
Liu, H.-X., Huang, Y., Xiao, G.-C., et al. 2021, RAA, 21, 070
Ma, X., Tao, L., Zhang, S.-N., et al. 2021, NatAs, 5, 94
Mao, D.-M., Yu, W.-F., Zhang, J.-J., et al. 2022, RAA, 22, 045009
Méndez, M., Karpouzas, K., García, F., et al. 2022, NatAs, 6, 577
Miller, J. M. 2007, ARA&A, 45, 441
Miller, J. M., Gendreau, K., Ludlam, R. M., et al. 2018, ApJL, 860, L28
Miyamoto, S., Kimura, K., Kitamoto, S., Dotani, T., & Ebisawa, K. 1991, ApJ, 383, 784
Miyasaka, H., Tomsick, J. A., Xu, Y., & Harrison, F. A. 2018, ATel, 12340, 1
Negoro, H., Nakajima, M., Sakamaki, A., et al. 2019, ATel, 12421, 1
Nowak, M. A. 2000, MNRAS, 318, 361
Oosterbroek, T., van der Klis, M., Vaughan, B., et al. 1996, A&A, 309, 781
Remillard, R. A., & McClintock, J. E. 2006, ARA&A, 44, 49
Remillard, R. A., Sobczak, G. J., Muno, M. P., & McClintock, J. E. 2002, ApJ, 564, 962
Revnivtsev, M., Sazonov, S., Churazov, E., et al. 2009, Natur, 458, 1142
Rout, S. K., Méndez, M., Belloni, T. M., & Vadawale, S. 2021, MNRAS, 505, 1213
Russell, D. M., Casella, P., Kalemci, E., et al. 2020, MNRAS, 495, 182
Schnittman, J. D., Homan, J., & Miller, J. M. 2006, ApJ, 642, 420
Stella, L., & Vietri, M. 1998, ApJ, 492, L59
Tomsick, J. A., Yamaoka, K., Corbel, S., et al. 2009, ApJL, 707, L87
van den Eijnden, J., Ludlam, R. M., Homan, J., et al. 2019, ATel, 12440, 1
Vignarca, F., Migliari, S., Belloni, T., Psaltis, D., & van der Klis, M. 2003, A&A, 397, 729
Walton, D. J., Mooley, K., King, A. L., et al. 2017, ApJ, 839, 110
Wang, J., Mastroserio, G., Kara, E., et al. 2021, ApJL, 910, L3
Xu, Y., Harrison, F. A., Tomsick, J. A., et al. 2020, ApJ, 893, 30
Xu, Y., Harrison, F. A., García, J. A., et al. 2018, ApJL, 852, L34
You, B., Bursa, M., & Życki, P. T. 2018, ApJ, 858, 82
You, B., Tuo, Y., Li, C., et al. 2021, NatCo, 12, 1025
Zhang, L., Altamirano, D., Uttley, P., et al. 2021, MNRAS, 505, 3823
Zhang, S.-N., Li, T., Lu, F., et al. 2020, SCPMA, 63, 249502
Zhang, W., Jahoda, K., Swank, J. H., Morgan, E. H., & Giles, A. B. 1995, ApJ, 449, 930
Zhou, D.-K., Zheng, S.-J., Song, L.-M., et al. 2021, RAA, 21, 005